Defect Passivation via the Incorporation of Tetrapropylammonium Cation Leading to Stability Enhancement in Lead Halide Perovskite

Anurag Krishna, Mohammad Ali Akhavan Kazemi, Michel Sliwa, G. N. Manjunatha Reddy, Laurent Delevoye, Olivier Lafon, Alexandre Felten, Mai Trang Do, Sébastien Gottis, Frédéric Sauvage

Defect passivation via the incorporation of tetrapropylammonium cation leading to stability enhancement in lead halide perovskite

Anurag Krishna[†], *Mohammad Ali Akhavan Kazemi*[†], *Michel Sliwa*[‡], *G. N. Manjunatha Reddy*[§], *Laurent Delevoye*[§], *Olivier Lafon*[§,‖], *Alexandre Felten*[#], *Mai Trang Do*[‡], *Sébastien Gottis*[†], *and Frédéric Sauvage*[†]*

[†]Laboratoire de Réactivité et Chimie des Solides (LRCS), CNRS UMR 7314 - Institut de Chimie de Picardie FR 3085, Université de Picardie Jules Verne, 33 rue Saint Leu, FR-80039 Amiens Cedex, France

[‡] Univ. Lille, CNRS, UMR 8516 - LASIR - Laboratoire de Spectrochimie Infrarouge et Raman, F-59000 Lille, France

[§] Univ. Lille, CNRS, Centrale Lille, ENSCL, Univ. Artois, UMR 8181−UCCS− Unité de Catalyse et Chimie du Solide, F-59000, Lille, France

[#] SIAM Platform, University of Namur, rue de Bruxelles 61, 5000 Namur, Belgium

[‖] Institut Universitaire de France, 1 rue Descartes, F-75231 Paris, France

Keywords: Perovskite solar cells stability, Defect passivation, time-resolved photoluminescence, solid-state NMR spectroscopy

ABSTRACT

Improving the performances of photovoltaic (PV) devices by suppressing non-radiative energy losses through the passivation of surface defects and enhancing perovskite solar cells stability to the level of standard PV materials represents one critical challenge in the field of perovskite solar cells. We report the beneficial features of introducing a tetrapropylammonium quaternary ammonium (TPA^+) cation that combines two key functionalities, namely surface passivation of $CH_3NH_3PbI_3$ nanocrystals through strong ionic/electrostatic interaction with the surface and bulk passivation via formation of type I heterostructure which acts as a barrier for recombination and reduces water ingress. As a result, non-encapsulated perovskite films with only 2 mol % of TPA^+ reached power conversion efficiencies over 17% under spectral irradiance corresponding to air mass (A.M.) 1.5G conditions. Furthermore, these films retain more than 85% of the initial

performance for over 1500 hours under ambient conditions, including a relative humidity of ~55±5%. The stability of these films is also significantly enhanced at 60 °C thermal stress or under 85% humidity storage. Perovskite thin films before and after the TPA^+ incorporation are characterized by X-ray diffraction, solid-state NMR spectroscopy, optical absorption spectroscopy and SEM imaging.

INTRODUCTION

Organic-inorganic metal halide ABX_3 perovskite solar cells (PSCs) have captivated the scientific community owing to their exceptional opto-electronic properties [1–5]. There has been an unprecedented growth in the field of perovskite-based photovoltaics (PV); for example, the power conversion efficiency (PCE) has augmented from 3.8% to over 25% [6]. The extended bandgap tunability of hybrid perovskite halides via a judicious control in the absorber's stoichiometry, in particular within $CH_3NH_3PbI_{3-x}X_x$ solid solution ($X = Br^-$ or Cl^-)[5], make them highly beneficial as a top cell tandem with crystalline silicon in order to cross the symbolic barrier of 30% [7]. In the context of these promising technological perspectives, three key issues remain to be addressed: (i) lead content and its potential solubility in real environment, (ii) process transfer from small (< 1 cm^2) to larger area (> 100 cm^2) with lower utilization of detrimental solvents, and (iii) to improve the stability of PSCs to reach the standards of silicon-based PV technology [8].

The archetypal three-dimensional (3D) perovskite-based on methylammonium lead halide composition ($MAPbI_3$) gathers the best in terms of opto-electronic characteristics but poorest in terms of stability due to its known thermal, moisture and light-induced degradation [8–10]. This limitation stems principally from the intrinsic volatile nature of the methylammonium cation

which is only in weak coulombic interactions within the inorganic framework[11]. More complex stoichiometries via the use of three different cations in the A-site and two distinct halide anions $Cs_x(FAPbI_3)_y(MAPbBr_3)_{1-x-y}$ perovskite has been developed to improve the stability and operational efficiency [12]. For instance, $Cs_x(MA_{0.17}FA_{0.83})_{(1-x)}Pb(I_{0.83}Br_{0.17})_3$ composition enabled PCEs over 20% while enhancing the thermal stability. However, such complex stoichiometries are metastable leading to phase segregation driven by halide demixing, thus losing gradually the unique opto-electronic properties of the original perovskite [13].

Depending on the deposition and the crystallization procedure (precursor concentration, annealing temperature and time, vapor treatment, antisolvent, etc.), the resulting film can contain different levels of grain boundaries and punctual defects, such as anionic vacancies or uncoordinated lead owing to their low formation energies. It translates into the formation of shallow traps that require their careful passivation to lower internal non-radiative energy losses and maximize the electron/hole diffusion length. The two kind of defects, extrinsic related to the film morphology and intrinsic related to crystallographic punctual defects, play a pivotal role not only for achieving high power conversion performances but also to reach long-term stability as they can facilitate oxygen and/or moisture ingress, thus accelerating the device degradation [14–16].

One credible approach to enhance the PSC's stability is the development of lower-dimensional structures derived from the Ruddlesden-Popper (LDRP) structure of composition $A'_{n-1}A_2B_nX_{3n+1}$, where A is the additional large organic cation (e.g., n-butyl ammonium, phenethylammonium or ethylenediammonium) and *n* represents the number of inorganic slabs separated by A. The large organic cations can more strongly interact with the inorganic $[PbI_6]^{4-}$ octahedra framework through hydrogen and ionic bonding, thus enhancing the overall structural robustness[17,18]. However, they have a stronger insulating character across the layers that

enhances quantum confinement. This leads to a larger bandgap (> 2 eV), a higher exciton binding energy (~300 meV)[19] and anisotropic charge transport, thus lowering solar cell performances with the highest PCE reported so far at ca. 13% [20–23].

Combining the high performances of the 3D perovskite with the stability of the 2D perovskite constitutes an essential stake in the technological and scientific roadmap of PSCs. Different approaches have been proposed so far, such as coating the 3D perovskite with a more stable 2D perovskite that can be moisture resistant [14,24–26] or mesostructuring 2D and 3D perovskites in the same volume [17,27–29].

In this work, we introduced the tetrapropylammonium cation (TPA^+) at the A-site along with methylammonium (MA^+) to create a mesoscale engineered absorber. The strategy behind the use of TPA^+, which is also a short-chain cationic surfactant, lies in its ability to strongly interact with the surface of the perovskite crystals through strong electrostatic and ionic interactions to stabilize the uncoordinated halide ions and to passivate surface defects [14,30]. As a result of these two functions, which are herein discussed on the basis of X-ray diffraction (XRD), solid-state NMR spectroscopy as well as time- and spatially-resolved UV-visible spectroscopies, films containing TPA^+ (< 4 mol %) exhibit longer excited-state lifetime and enhanced luminescence homogeneity at mesoscale than films with no TPA^+. Optimized PV devices based on quaternary ammonium reached PCE over 17% under air mass (A.M.) 1.5G conditions while drastically reinforcing the device stability against humidity, temperature and light stress without any means of external encapsulation.

RESULTS AND DISCUSSION

Tetrapropylammonium iodide (TPAI) was added to the perovskite precursor solution containing MAI and PbI_2, in order to create a MA^+ deficient film including TPA^+ cations with a molar fraction of either 2 or 4 mol%. This leads to a mixed-phase perovskite of general formula $TPA_xMA_{1-x}PbI_3$ assuming the stoichiometry in solution to be kept in the film. The molar fractions exceeding 4 mol % of TPAI leads to morphological issues of the resulting film, which exhibits cracks and voids. To gain insight into the morphology and crystallinity of $MAPbI_3$ (MAPI) thin films before and after the incorporation of TPA^+ cations, XRD measurements were conducted, analyzed and compared. All of these three films, $MAPbI_3$, $TPA_xMA_{1-x}PbI_3$ 2% and $TPA_xMA_{1-x}PbI_3$ 4% showed a strong preferential orientation along the (110) plane, indicating that the long (001) axis of the tetragonal unit cell is mainly perpendicular to the substrate (Figure 1a). This preferential growth, corresponding to the dense lead and iodide facets of the crystal structure, is typically encountered in high-quality perovskite films, thus providing the best performances in terms of charge collection, PCE and photoluminescence quantum yield [31–33]. For the reference MAPI, an additional diffraction peak at $2\theta = 12.7°$ is observed. This latter is assigned to the (001) plane of the hexagonal PbI_2 phase, which originates from the 9 mol. % excess of PbI_2 introduced for the film preparation to optimize the PCE of MAPI as demonstrated in the literature [34]. At 2% and 4% of TPA^+, the intensity of the PbI_2 diffraction peak at 12.7° diminishes which means that TPAI reacts with the excess of PbI_2 (Figure 1b). A new diffraction peak appears at a lower angle, $2\theta = 8.1°$ (Figure 1c). This new peak, which cannot be indexed into the conventional tetragonal unit cell of I4/mcm space group, is attributed to an intermediate $TPAPb_4I_9$ phase formed in the presence of excess of PbI_2, until this latter is totally consumed (Supporting Information, Figure S1). This confirms the interactions between TPA^+ cations and lead iodide framework, in particular with iodide anions to which TPA^+ can bind strongly [30]. By

comparison, in lead iodide perovskite, the resulting PbI_3^- frameworks can only accommodate the smallest organic cations such as methylammonium (r_{eff} = 217 pm) and formamidinium (r_{eff} = 252 pm) based on the Goldschmidt tolerance factor [35]. Larger moieties at the A-site conducts to the formation of a lower dimensional layered structures [36]. In the case of TPA^+, which has a an ionic radius of 450 pm [37], the Goldschmidt tolerance factor is equal to 1.4 and TPA^+ cannot be accommodated inside the lattice of the perovskite structure [20,21,27]. However, although this latter cannot be accommodated, TPA^+ modifies the MAPI lattice. Indeed, a full pattern matching refinement of the MAPI lattice cell parameters has been carried out to evaluate the influence of MAPI lattice cell upon the addition of TPA^+. Interestingly, the addition of TPA^+ provokes a reduction of the cell volume mostly driven by a shrinkage along the (001) direction: (a = 8.8725(2) Å, c = 12.6253(13) Å, V = 993.89(8) $Å^3$) and (a = 8.8720(1) Å, c = 12.6272(10) Å, V = 993.93(8) $Å^3$) for 2 and 4 mol % TPA^+ compared to (a = 8.8748(1) Å, c = 12.6591(5) Å, V = 997.06(4) $Å^3$) for pure MAPI (Supporting Information, Table S1). This is an additional evidence supporting that TPA^+ is not incorporated within the lattice as otherwise it would have yielded to a cell volume expansion [29]. These results suggest that the obtained MAPI film has not exactly same stoichiometry. It is expected to be MA^+ deficient. Though, *a priori*, it cannot be ruled out that the TPA^+ constrains the MAPI lattice leading to the formation of TPA^+ rich domains and $TPAPb_4I_9$ domains that are likely to be located at grain boundaries [29]. This second hypothesis is consistent on the one hand with a well-visible crystallite size reduction along (110) plane from 185 nm for MAPI to 130 and 131 nm for $(TPA)_x(MA)_{1-x}PbI_3$ 2% and $(TPA)_x(MA)_{1-x}PbI_3$ 4%, respectively (using Scherrer's equation after subtraction of the instrumental broadening) and on the other hand with the reduction of the particle's size observed by Scanning Electron Microscopy (SEM) (Figure 2). The substitution of MA^+ by TPA^+ helps to enhance the film's

quality with a clear reduction of pinholes and less pronounced grain boundaries leading to a more compact, more homogeneous and denser films which result from the surfactant property of TPA^+.

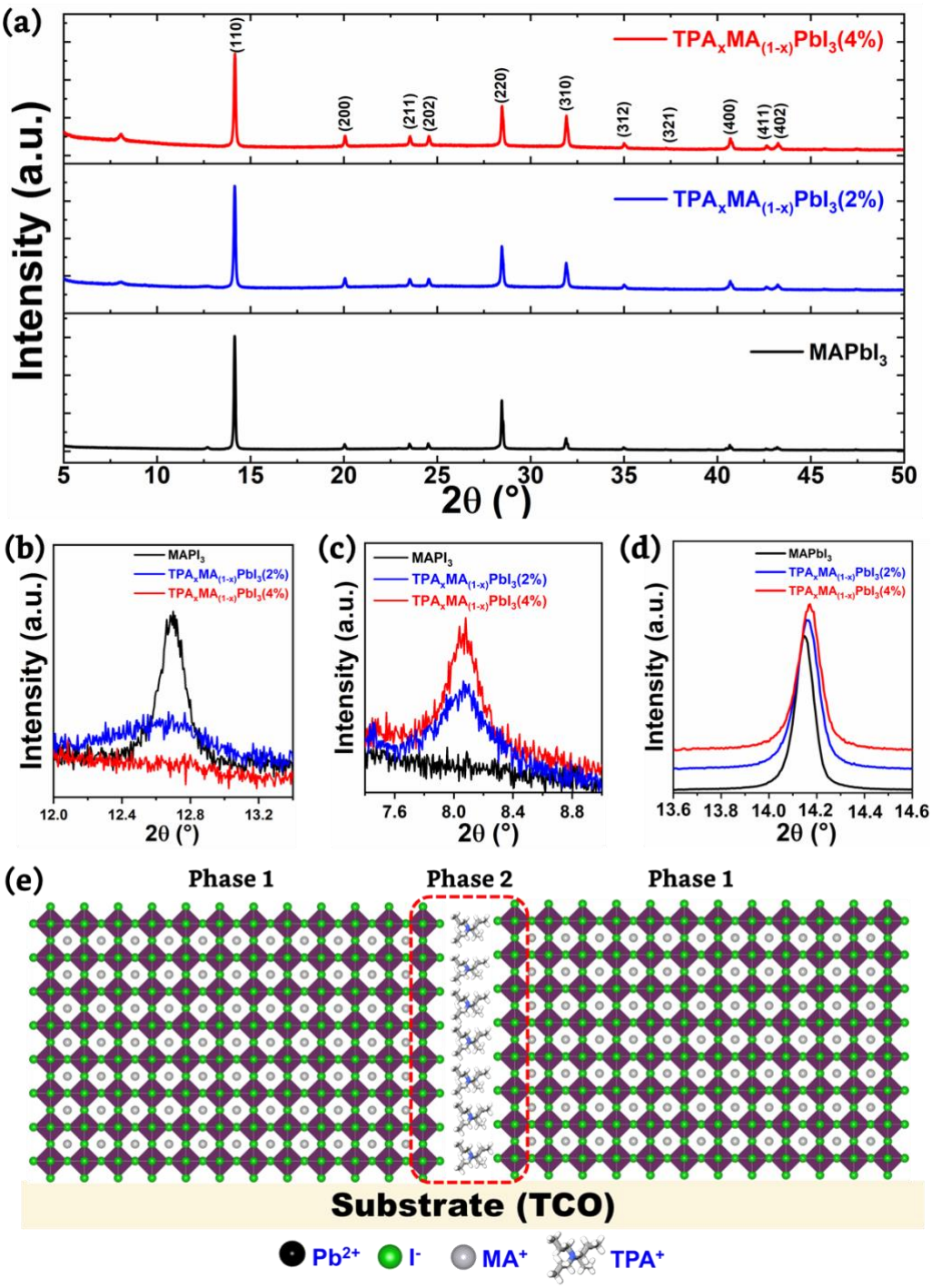

Figure 1. (a) Comparison of the XRD patterns of MAPI and $TPA_xMA_{1-x}PbI_3$ 2% and 4% films. (b-d) Inset of the evolution of PbI_2 (001) diffraction peak at 12.7°, new intermediate phase at 8.1° and (110) diffraction peak upon addition of TPAI. (e) Schematic showing the self-assembled mixed phase structure.

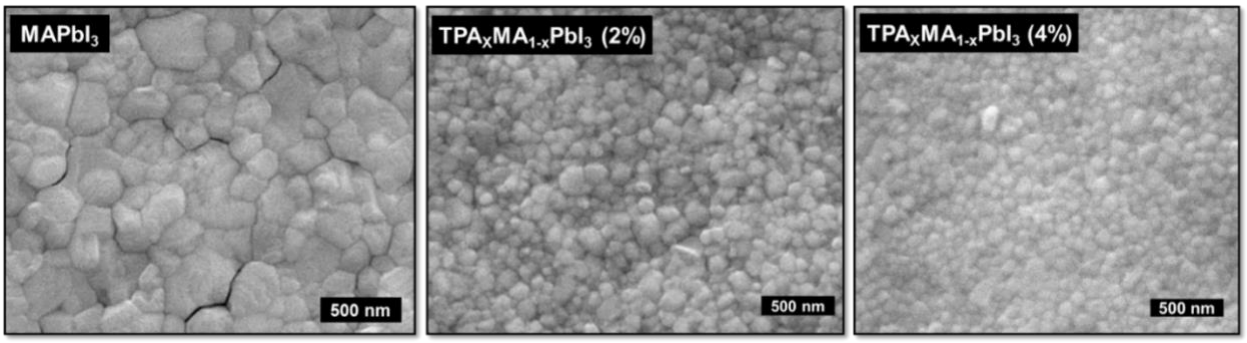

Figure 2. Morphology of Perovskites: Top view scanning electron microscopy images at same magnification of MAPI, $TPA_xMA_{1-x}PbI_3$ 2% and 4% films deposited on a glass substrate.

To further examine the location of TPA^+ cation in the perovskite materials, we acquired 1D and 2D ^1H solid-state NMR spectra of $TPA_xMA_{1-x}PbI_3$ 4% and its precursor TPAI. The local environments of cations in mixed cations lead halide perovskites has recently been examined using solid-state NMR spectroscopy [*Cite: Kubicki, D. J. et al, JACS,* ***2017****, 139, 14173* ***&*** *Van Gompel, W. T. M. et al J. Phys. Chem. C* ***2018****, 122, 4171* ***&*** *Kubicki, D. J. et al, JACS,* ***2018****, 140, 3345* ***&*** *Bi, D. et al., Nature Communications* ***2018,*** *9 (1), 4482*], and especially of protons [*Franssen, W. M. J. et al ChemPhysChem* ***2018****, 19, 3107* ***&*** *Milić, J. V. et al., Advanced Energy Materials* ***2019,*** *0 (0), 1900284* ***&*** *Franssen, W. M. J., Kentgens, A. Solid State Nucl. Magn. Reson.* ***2019****, 100, 36* ***&*** *Alharbi, E. A. et al.., Nature Communications* ***2019,*** *10 (1), 3008* ***&*** *Alazani, A. Q. et al JACS DOI: 10.1021/jacs.9b07381*]. The 1D ^1H MAS NMR spectrum of $TPA_xMA_{1-x}PbI_3$ 4% is displayed in Figure 3a. This spectrum is dominated by the signals of

ammonium and methyl groups of MA^+ cations, resonating at 6.5 and 3.5 ppm, respectively. However, three additional weaker signals, at 4.8, 1.3 and 0.9 ppm, are assigned to NCH_2, CH_2 and CH_3 protons of TPA^+. The relative integrated intensities of MA^+ and TPA^+ signals are consistent with the molar fraction of 4 mol% in TPA^+. This NMR result indicates that the perovskite film has the same stoichiometry as the solution. Furthermore, the isotropic chemical shifts of NCH_2 (4.8 ppm) and CH_2 (1.3 ppm) protons of TPA^+ are deshielded and shielded, respectively, with respect to the ^1H signals in the pure of TPAI phase (NCH_2, 2.5-4.5 ppm and CH_2, 1.8 ppm). These different chemical shifts indicate distinct atomic-level environments of TPA^+ cations in $TPA_xMA_{1-x}PbI_3$ 4% and pristine TPAI phase, which are consistent with a mixing at microscopic level of TPA^+ cations and MAPI phase, as shown in Figure 1e. Furthermore, the ^1H signals of TPA^+ cations are narrower for $TPA_xMA_{1-x}PbI_3$ 4% than the TPAI phase. Such a narrowing is consistent with a close proximity between TPA^+ cations and lead iodide octahedra, which result in smaller intermolecular ^1H-^1H dipolar couplings for the TPA^+ protons.

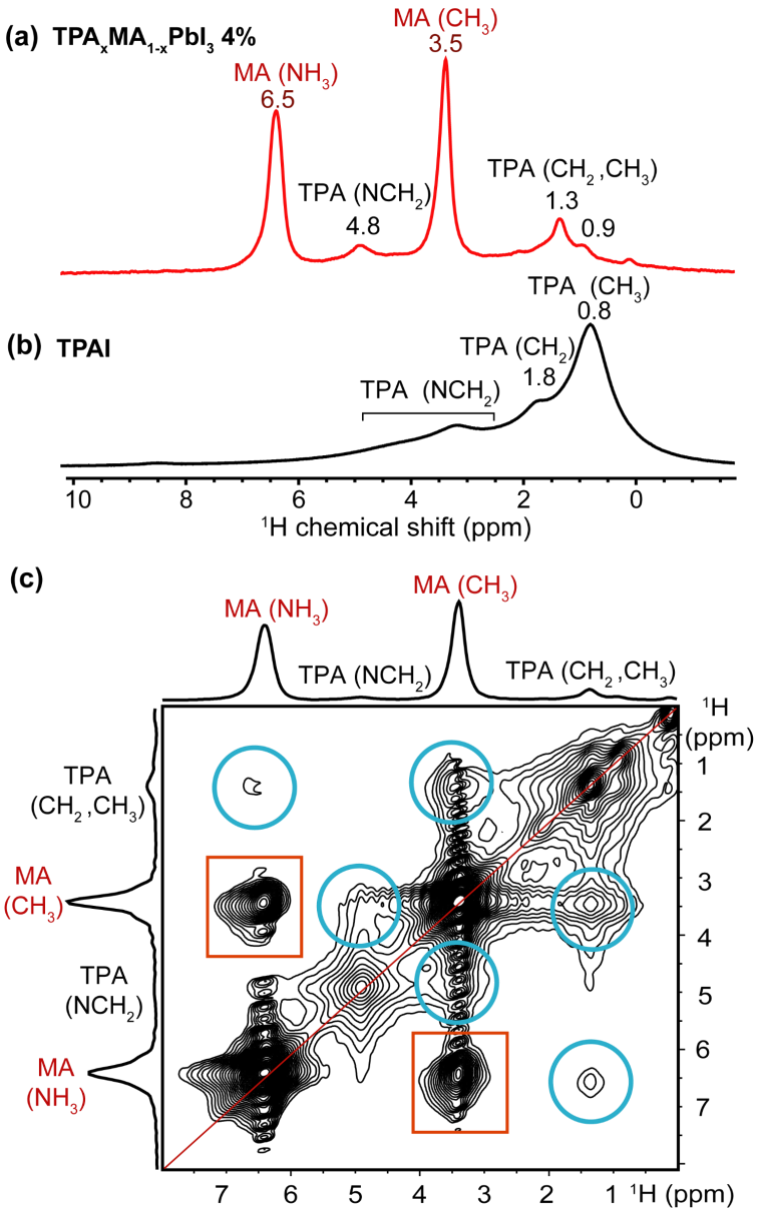

Figure 3. Solid-state 1D ^{1}H MAS NMR spectra of (a) $TPA_xMA_{1-x}PbI_3$ 4% and (b) TPAI precursor acquired at 18.8 T with MAS frequencies of 35 and 60 kHz MAS, respectively. (c) 2D ^{1}H-^{1}H spin-diffusion NMR spectrum of $TPA_xMA_{1-x}PbI_3$ 4% acquired at 18.8 T with a MAS frequency of 35 kHz using τ_{mix} = 100 ms. The red rectangles and the cyan circles indicate the cross-peaks corresponding to intra-molecular ^{1}H-^{1}H dipolar interactions in MA^+ cations and inter-molecular ones between MA^+ and TPA^+ cations, respectively.

To further corrobate the mixing of TPA^+ cations and MAPI at microscopic level, we carried out two-dimensional (2D) ^1H-^1H spin-diffusion NMR experiments on $TPA_xMA_{1-x}PbI_3$ 4% using various mixing times, τ_{mix} (see Figure 3c and Supporting Information, Figure S2) [*Cite: Elena, B. et al., Journal of the American Chemical Society* ***2006,*** *128 (29), 9555-9560* ***&*** *Milić, J. V. et al., Advanced Energy Materials* ***2019,*** *0 (0), 1900284* ***&*** *Alharbi, E. A. et al.., Nature Communications* ***2019,*** *10 (1), 3008* ***&*** *Alazani, A. Q. et al JACS DOI: 10.1021/jacs.9b07381*]. For τ_{mix} = 1 ms, the 2D ^1H-^1H spin-diffusion spectrum only contains diagonal peaks, corresponding to the signals in the 1D ^1H NMR spectrum (see Supporting Information, Figure S2a), i.e. no magnetization exchange between the various proton sites occurs during the mixing time. For $\tau_{mix} \geq 10$ ms, cross-peaks are detected, which evidence the exchange of magnetization between different proton sites via ^1H-^1H spin diffusion. The intensity of these cross-peaks increases for increasing mixing time. For hybrid perovskites, the cross-peaks can only be observed when the correlated protons are distant by less than a few nanometers. The spectra acquired using $\tau_{mix} \geq 100$ ms exhibit cross-peaks arising from intra-molecular proximities between ammonium and methyl protons in MA^+ cations as well as inter-molecular ones between the protons of MA^+ and TPA^+ cations. These inter-molecular cross-peaks prove unambiguously that TPA^+ and MA^+ are microscopically mixed within the same phase, as shown on Figure 1c. The cross-peaks between TPA^+ protons are not visible even for τ_{mix} = 500 ms because of the low molar fraction of TPA^+ cations. We also acquired 2D ^1H through-space double-quantum (DQ)-single quantum (SQ) homonuclear correlation NMR spectrum of the $TPA_xMA_{1-x}PbI_3$ 4% (Supporting Information, Figure S3a). Signals in this 2D spectrum are only observed for protons distant by less than 0.5 nm. The signals located on the DQ diagonal, the auto-correlation peaks, reveal proximities between protons with similar isotropic chemical shifts, whereas the off-

diagonal signals, the correlation peaks, correspond to proximities between sites with distinct isotropic chemical shifts. In the case of $TPA_xMA_{1-x}PbI_3$ 4%, the ^1H through-space DQ-SQ correlation spectrum is dominated by the auto-correlation peaks of CH_3 and NH_3 groups in MA^+ cations as well as the correlation peaks between these two distinct ^1H resonances. The spectrum also contains auto-correlation peaks of TPA^+ cations. Nevertheless, no correlation peak between ^1H signals of MA^+ and TPA^+ cations can be seen. Hence, MA^+ and TPA^+ protons must be distant by more than 0.5 nm and as shown in Figure 1c, TPA^+ cations must interact with the lead iodide octahedra but not with the MA^+ cations.

The opto-electronic properties of the MAPI and $TPA_xMA_{1-x}PbI_3$ perovskite films were investigated by steady-state UV-visible absorption spectroscopy and the position of the valence band determined by Ultraviolet Photon-electron Spectroscopy (UPS) (Figure 4). Regardless of TPA^+ content in the film, there is no significant change in both the absorption spectra and energy onset (Figure 4a). The Tauc plot, assuming a direct allowed transition in lead halide perovskite, leads to an optical bandgap value of 1.59 eV for all the samples (Figure 4c-e). The bandgap of the second phase $TPAPb_4I_9$ has been determined to be 2.66 eV (Supporting Information, Figure S4). The Urbach energy, E_u, was determined using [38].

$$\ln(\alpha) = \ln(\alpha_0) + \frac{h\nu}{E_u} \qquad (1)$$

where α is the absorption coefficient (cm^{-1}), α_0 is a constant and $h\nu$ is the photon energy (eV) absorbed in the tail states. Interestingly, one role of TPA^+ is to alleviate the electronic disorder and surface defects as demonstrated by the lowering in the Urbach energy from 83.6 meV for MAPI to 53.2 meV and 64.1 meV for $TPA_xMA_{1-x}PbI_3$ 2% and $TPA_xMA_{1-x}PbI_3$ 4%, respectively [38,39]. UPS measurements were carried out to determine the work function and valence band maximum (VBM) position of MAPI and $TPA_xMA_{1-x}PbI_3$ 2% from a linear extrapolation of the

secondary electron cutoff (Figure 4f-h). The work function for MAPI and $TPA_xMA_{1-x}PbI_3$ 2% was determined to be at 4.23 eV and 4.08 eV, respectively. The value of the work function for MAPI is in agreement with what has been previously reported in the literature [40]. The shift of this latter in $TPA_xMA_{1-x}PbI_3$ 2% stems from an upward movement of the Fermi level in the gap as a result from different punctual defect levels in the film [41,42]. This shift towards ca. 4.10 eV value is also interesting as it tends to suggest a lower level of p-type defects induced by the inclusion of TPA^+ in good agreement with the studies reported by Duhm et al [41]. Figure 3h schematize the band diagram based on UPS measurements. The VBM position has been determined by the extrapolation of the UPS data plotted on a logarithmic scale[43,44], and is equal to 1.56 eV and 1.58 eV for MAPI and $TPA_xMA_{1-x}PbI_3$ 2%, respectively (Figure 4g). For $TPA_xMA_{1-x}PbI_3$ 4%, the reproducibility of such measurements was infeasible due to excessive surface charging effects.

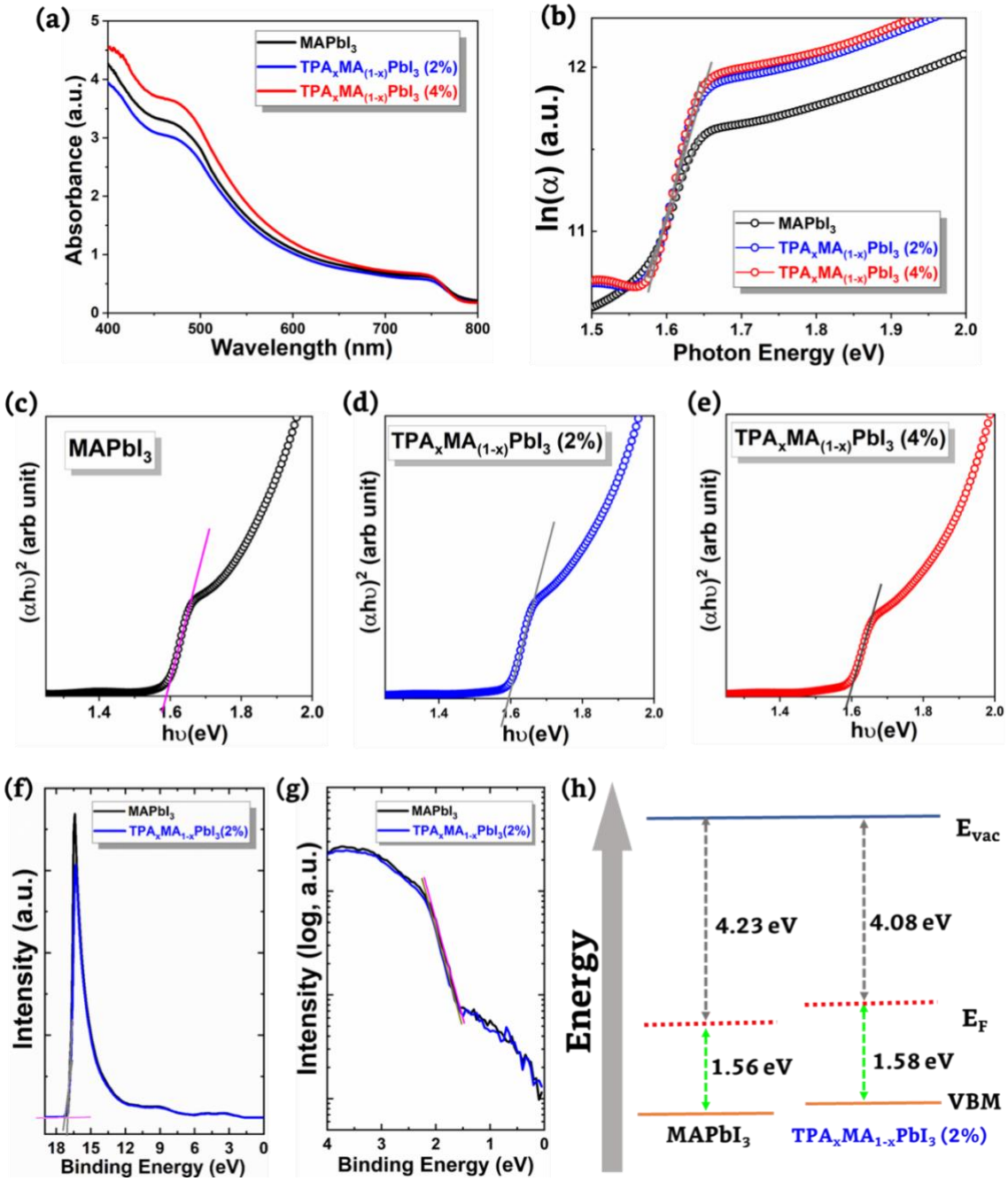

Figure 4. Comparison between MAPI, $TPA_xMA_{1-x}PbI_3$ 2% and $TPA_xMA_{1-x}PbI_3$ 4% of (a) steady-state UV-visible absorption spectra; (b) Urbach plot and (c-e) Tauc plot. (f) The secondary electron cutoff of MAPI and $TPA_xMA_{1-x}PbI_3$ 2% in UPS measurements; (g) Comparison of UPS measurements in the valence band maximum (VBM) region of MAPI and $TPA_xMA_{1-x}PbI_3$ 2% and (h) schematic of the energy levels of the corresponding samples.

Steady-state photoluminescence (PL) and time-correlated single-photon counting (TCSPC) measurements were carried out to evaluate the modifications in charge carrier dynamics (Figure 5). The steady-state PL yield of $TPA_xMA_{1-x}PbI_3$ 2% and $TPA_xMA_{1-x}PbI_3$ 4% films were observed to be four and six times larger than that of MAPI, respectively (Supporting Information, Table S2). This indicates that the addition of TPA^+ cations leads to successful passivation of non-radiative shallow traps. Interestingly, regardless of the amount of TPA^+ in the film, we have no evidence of PL fingerprint from the secondary phase in the range of 300 – 650 nm excitation and 350 – 850 nm emission (Supporting Information, Figure S5). We evaluated the PL lifetime of MAPI, $TPA_xMA_{1-x}PbI_3$ 2% and $TPA_xMA_{1-x}PbI_3$ 4% films using TCSPC technique (Figure 5b). The PL decay in MAPI perovskite is usually assigned to second order kinetic radiative bimolecular recombination[45–47]. All PL decays were reconvoluted using a bi-exponential function which is commonly used to describe radiative recombination in perovskites, in particular when PbI_2 in excess is introduced in association with an excitation lower than ca. 500 nm [47–49]. The different values of amplitude, characteristic lifetimes and average lifetime extracted are summarized in Table 1.

Table 1: Summary of lifetime decays determined from the fit to the equations given in the Supporting Information of the TCSPC data displayed in Figure 5b acquired using an excitation wavelength of 475 nm (2 MHz, fluence ca. 100 nJ/cm^2), an emission wavelength of 770 nm with 10 nm slit size and a long pass filter of 645 nm.

Parameters	**$MAPbI_3$**	**$TPA_xMA_{1-x}PbI_3$ (2%)**	**$TPA_xMA_{1-x}PbI_3$ (4%)**
A_1	10940	5009	2016
α_1 (%)	24.2	3.1	3.5
τ_1 (ns)	9.9	6.1	7.2
A_2	6997	14641	4830

α_2 (%)	75.8	96.9	96.5
τ_2 (ns)	48.4	65.1	83.3
$<\tau_{av}>$ (ns)	39.1	63.2	80.7

The introduction of TPA^+ in the film leads to a noticeable reduction of the fast contribution from 24% to ca. 3%. This is attributed in main part to the consumption of PbI_2 excess in the film in agreement with recent assignments by Scheblykin et al.[49]. This amplitude reduction of this fast component comes with a longer lifetime of the second contribution from 76 ns to ca. 97 ns, thus signifying that TPA-based films reduces bimolecular radiative recombination dynamics. As a result, we determined the average PL lifetime of the $TPA_xMA_{1-x}PbI_3$ 2% and $TPA_xMA_{1-x}PbI_3$ 4% to be 63.2 ns and 80.7 ns, respectively. These values are about two times greater than pure $MAPbI_3$ which is in our case 39.1 ns. This average value is in agreement with the literature for a pure MAPI film excited in the blue region. All these results confirm the interfacial role of TPA^+ in the suppression of non-radiative monomolecular recombination and prolonging the dynamics of bimolecular radiative recombination, hence conferring improved electronic properties of the perovskite film. We hypothesize that the second phase $TPAPb_4I_9$ is formed at the grain boundaries. As aforementioned, the bandgap of MAPI and $TPAPb_4I_9$ is 1.59 eV and 2.66 eV, respectively. Due to this narrow and wider bandgap configuration, it forms a type-I heterostructure as schematized in Figure 5c[50]. In such a type-I heterostructure, when the carriers from MAPI grains are reaching the interface, the electrons-holes (e^-/h^+) carriers are maintained in the bulk of MAPI without suffering from recombination between particles at the grain boundaries owing to interfacial energetic mismatch [29,51]. In other words, the second phase formed upon addition of TPA^+ acts as a barrier to prevent the recombination.

Figure 5. Charge carrier dynamics: (a) steady-state PL measured at 450 nm excitation wavelength; (b) TCSPC decay of MAPI, $TPA_xMA_{1-x}PbI_3$ 2% and $TPA_xMA_{1-x}PbI_3$ 4% at 475 nm excitation (2 MHz, 100 nJ/cm^2 fluence) and at 770 nm emission with a 645 nm long pass filter. The films were deposited on a glass substrate and excited from the perovskite side. (c) The coexistence of $TPAPb_4I_9$ and $MAPbI_3$ perovskite in the film shows a type I alignment of the band edge, with the bandgap of 2.66 and 1.59 eV, respectively.

Fluorescence lifetime imaging microscopy (FLIM) was used to get further insights into bulk lifetimes, defects and film heterogeneity as previously discussed by deQuilettes et al.[47]. We measured different area in the films cartography representative of fluorescence intensity and lifetimes. As shown in Figure 6, the quantum yield of luminescence is increasing with the

percentage of TPA^+ in agreement with steady-state and TCSPC experiments. From the average lifetime images (in intensity), we can conclude that the increase of intensity stems from a drastic enhancement in the film's homogeneity associated to the passivation of the surface trap states by TPA^+. Indeed, whereas $MAPbI_3$ films are clearly heterogeneous in both the terms of photo-luminescence yield and in average lifetimes (Supporting Information, Figure S6), $TPA_xMA_{(1-x)}PbI_3$ 4% becomes very homogenous within the spatial resolution of the FLIM experiments, with an average lifetime about 5 times greater than $MAPbI_3$ in agreement with previous TCSPC study.

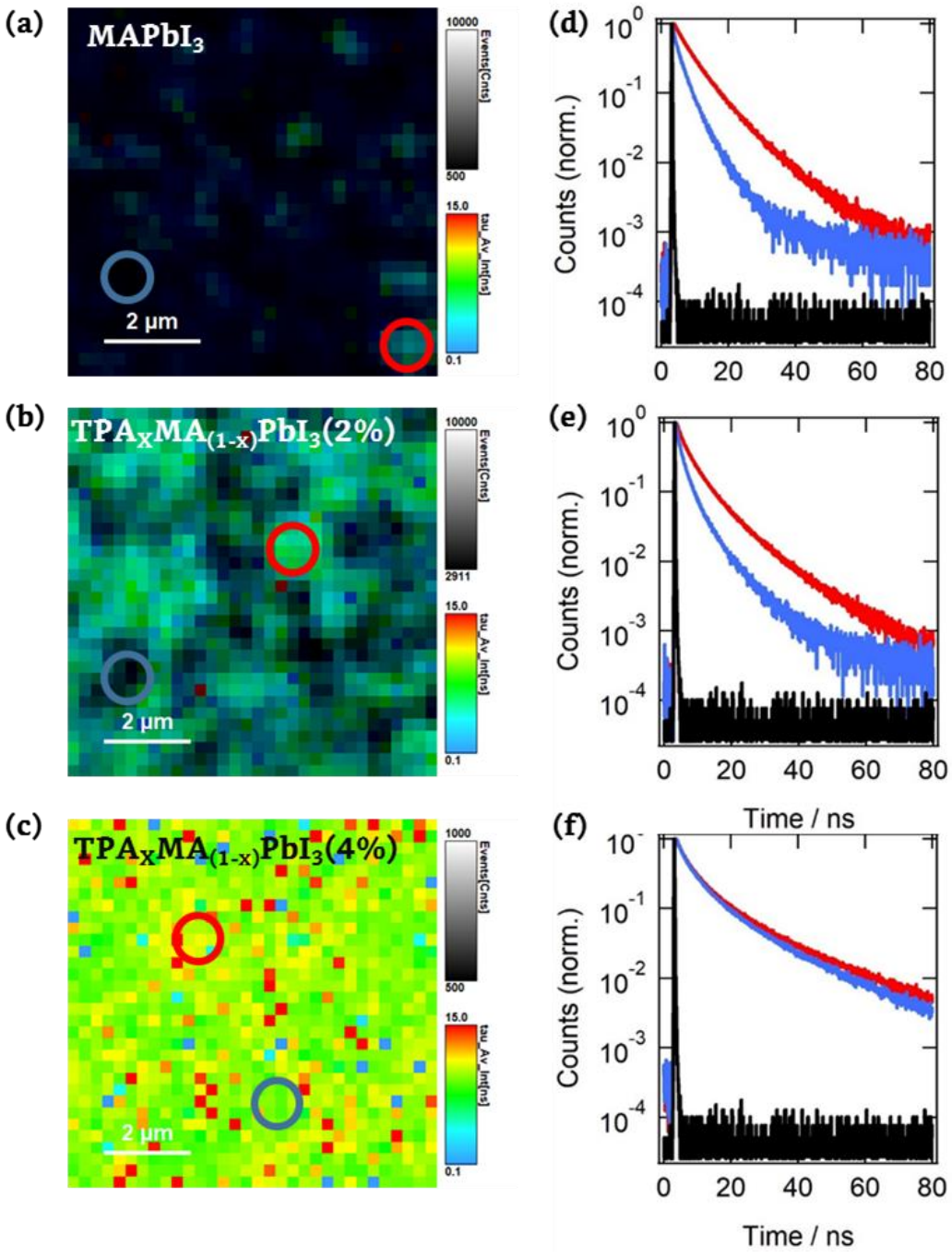

Figure 6. Fluorescence lifetime imaging: Counts and average lifetime for a 8 µm by 8 µm image (128 by 128 pixels) of (a) $MAPbI_3$, (b) $TPA_xMA_{(1-x)}PbI_3$ 2% and (c) $TPA_xMA_{(1-x)}PbI_3$ 4%. Measured decays (until to reach about 104 at the maximum counts) for a pixel in the region with high (red) and low counts (blue) for (d) $MAPbI_3$, (e) $TPA_xMA_{(1-x)}PbI_3$ (2%) and (f) $TPA_xMA_{(1-x)}PbI_3$ (4%). 470 nm laser is used for excitation (100 ps FWHM, 2 MHz, 5 µJ.cm^2 and photons higher than 650 nm were detected).

To gain insight into the beneficial effect of the addition of TPA^+ cation on the photovoltaic performances and on the device stability, we adopted the following device architecture: fluorine-doped tin oxide (FTO)/blocking (bl) layer-TiO_2/mesoporous (mp)-TiO_2/perovskite/spiro-OMeTAD/Au. Figure 7a shows the current density-voltage (J-V) curves of the champion device recorded under A.M. 1.5G conditions (100 mW/cm^2) based on MAPI, $(TPA)_x(MA)_{1-x}PbI_3$ 2% and $(TPA)_x(MA)_{1-x}PbI_3$ 4% under reverse scan. The corresponding open-circuit photovoltage (V_{OC}), short-circuit current density (J_{SC}), fill factor (FF) and power conversion efficiency (PCE) are summarized in Table 2. The statistical distribution of the photovoltaic characteristics (J_{SC}, V_{OC}, FF, and PCE) from at least 15 devices of each composition is presented in Figure 7b-e. As a result, MAPI, $(TPA)_x(MA)_{1-x}PbI_3$ 2% and $(TPA)_x(MA)_{1-x}PbI_3$ 4% showed a maximum PCE of 17.1%, 17.2% and 16.5%, respectively. This suggests that the introduction of TPA^+ leading to the formation of $TPAPb_4I_9$ intermediate phase does not impede the charge collection at this molar level. The main feature of TPA^+ for device performance is related to the reduction of internal energy losses. This translates into an enhancement of the cell photo-voltage from 0.972 V (±0.019 V) for MAPI to 1.02 V (±0.013V) and 1.04 V (±0.014 V) for $(TPA)_x(MA)_{1-x}PbI_3$ 2% and $(TPA)_x(MA)_{1-x}PbI_3$ 4%, respectively. This is attributed to the suppression of non-radiative recombination due to the passivation of defects by addition of TPA^+ and the longer lifetimes which raise up the quasi-Fermi level in TiO_2 nanocrystals [52].

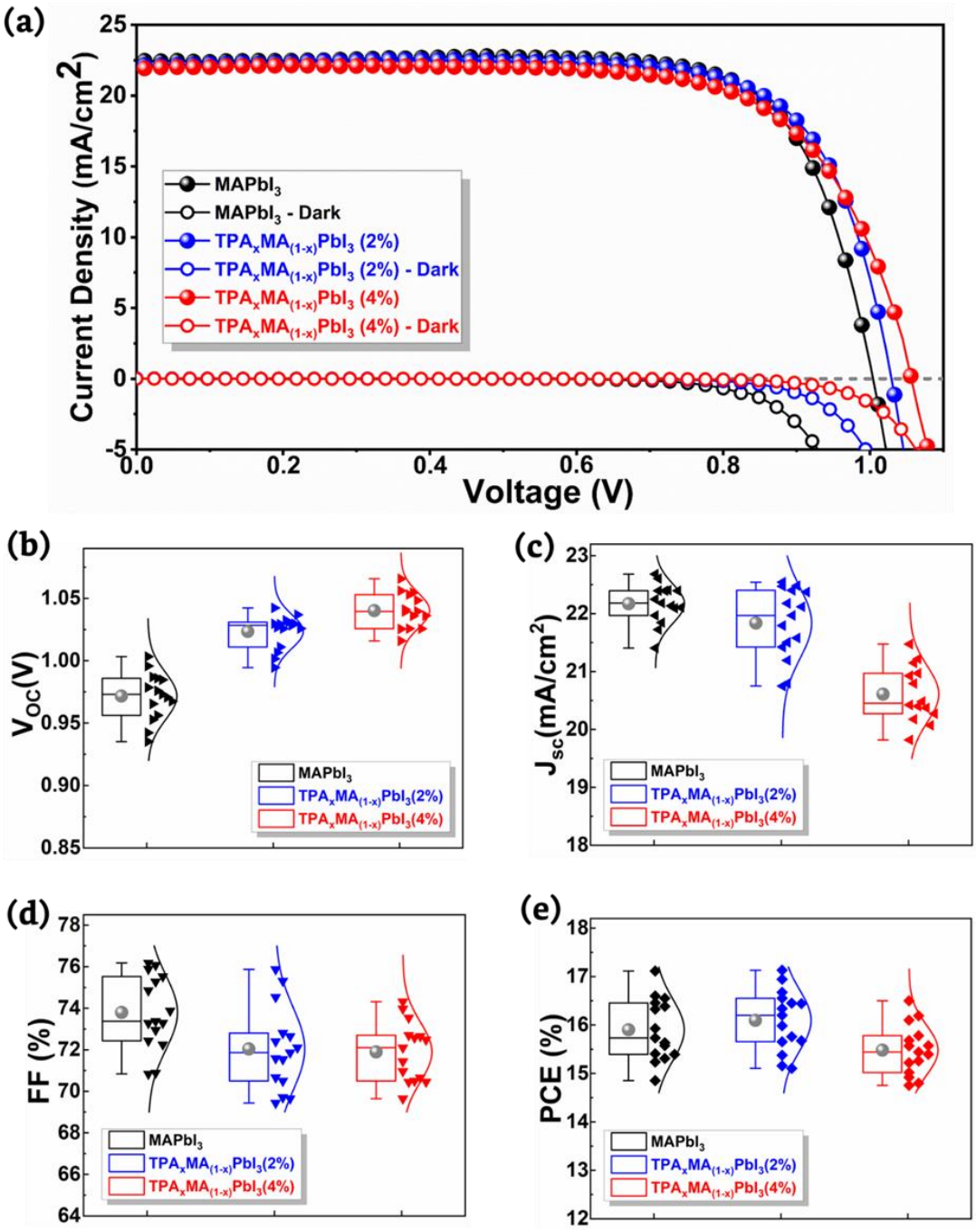

Figure 7. Device performances and statistics: (a) (J–V) curve of the champion cell prepared with MAPI, $TPA_xMA_{1-x}PbI_3$ 2% and $TPA_xMA_{1-x}PbI_3$ 4% under 3A class Xenon sun simulator at A.M. 1.5G conditions; Statistical data over at least 15 cells for (b) V_{OC}, (c) J_{SC} (d) FF and (e) PCE values for MAPI, $TPA_xMA_{1-x}PbI_3$ 2% and $TPA_xMA_{1-x}PbI_3$ 4%

Table 2. Summary of photovoltaic characteristics for devices based on MAPI, $TPA_xMA_{1-x}PbI_3$ 2%, and $TPA_xMA_{1-x}PbI_3$ 4% perovskites. In bracket is the average value including standard deviation (scan rate: 10 mV/s; without any prior light soaking or pre-treatment applied to cell).

Devices	V_{OC} (V)	Jsc (mA/cm^2)	FF (%)	PCE (%)
$MAPbI_3$	1.00 (0.972±0.019)	22.4 (22.17±0.33)	76.2 (73.8±1.78)	17.1 (15.9±0.64)
$TPA_XMA_{1-x}PbI_3$ (2%)	1.03 (1.02±0.013)	22.1 (21.84±0.61)	75.3 (72.05±2)	17.2 (16.1±0.63)
$TPA_XMA_{1-x}PbI_3$ (4%)	1.05 (1.04±0.014)	21.8 (20.61±0.48)	72.1 (71.9±1.43)	16.5 (15.5±0.52)

The motivation behind TPA^+ incorporation lies in a possible improvement of the device stability without any means of external encapsulation. Figure 8a compares the device stability under argon atmosphere and ambient conditions (T ~25 °C). The control devices based on MAPI degraded after 400 hours ageing, leading to only 30% power conversion efficiency retention after 2000 hours ageing. By contrast, the devices based on $(TPA)_x(MA)_{1-x}PbI_3$ 2% and $(TPA)_x(MA)_{1-x}PbI_3$ 4% retained 90% and 93% of initial PCE under same conditions. This remarkable stability improvement is also confirmed under more realistic storage conditions such as moisture (RH ~55±5%), elevated temperature of up to 60 °C and ambient light exposure (Figure 8b,c). In such conditions, MAPI device showed a monotonous fading of initial performance during the first 400 hours leading to a complete loss of performances after ca. 1300 hours of ageing. By comparison, $(TPA)_x(MA)_{1-x}PbI_3$ 2% and $(TPA)_x(MA)_{1-x}PbI_3$ 4% maintained 80% PCE retention after ca. 1100 hours and 1900 hours, respectively (Figure 8b). Furthermore, device stability improvement by means of TPA^+ addition is also confirmed at higher storage temperature, i.e. 60 °C in argon

atmosphere (Figure 8c). The argon atmosphere was chosen to avoid degradation from other device components, in particular the hole transporting materials (HTM) which becomes oxygen and moisture sensitive [53]. The MAPI device losses 50% of its initial PCE after 500 hours ageing. By contrast, $(TPA)_x(MA)_{1-x}PbI_3$ 2% and $(TPA)_x(MA)_{1-x}PbI_3$ 4% can maintain their efficiencies as high as 84% and 86% retention under the same conditions. Stability enhancement by the means of substitution by TPA^+ represents a step forward towards the current state of the art stability in the field. Our work supports that the stability enhancement upon addition of TPA^+ cation in the film is the result of internal factors such as higher hydrophobicity of the film and external key factors such as denser and fewer defect crystals and grain boundaries since the onset of perovskite degradation is likely proceeding via active defects and grain boundaries [54].

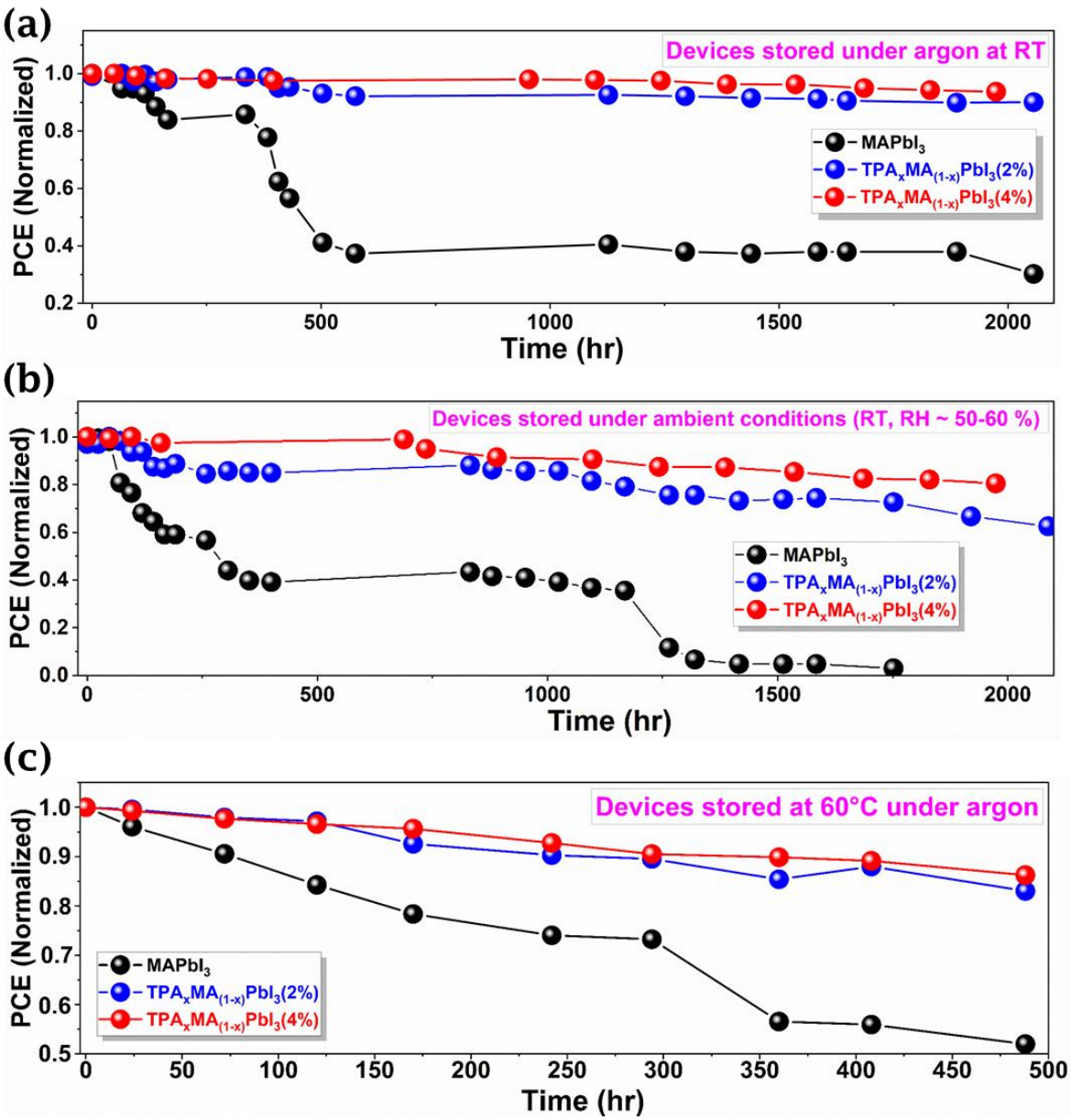

Figure 8. Stability of perovskite solar cells: Stability assessment of non-encapsulated perovskite solar cells based on MAPI, $(TPA)_x(MA)_{1-x}PbI_3$ 2% and $(TPA)_x(MA)_{1-x}PbI_3$ 4% (a) under 25 °C in argon over 2000 hours. The initial PCE of the devices were 16.6%, 16.7%, and 16.2%, respectively; (b) under 25 °C over 2000 hours with RH of 55±5% under ambient light. The initial PCE of the devices were 16.3%, 16.4%, and 16.0 %, respectively; (c) at 60 °C under argon for 500 hours. The initial PCE of the devices were 16.2%, 16.4%, and 16.5%, respectively.

Stability assessment of full devices under stringent humidity conditions remains from the point of view of absorber's side as well as from the hole transporter (HTM)[55]. Indeed, most of

HTMs required to be doped by means of air-sensitive and highly hygroscopic oxidizing dopants which catalyze the solar cell degradation[56]. Interestingly, we demonstrate in this work that a small inclusion of TPA^+ in the film allows to drastically reduce the perovskite decomposition into PbI_2 under 85% atmospheric humidity. The comparison of XRD patterns (Figure 9) enabled to identify the changes in long-range structural order in aged MAPI (a), $(TPA)_x(MA)_{1-x}PbI_3$ 2% (b) and $(TPA)_x(MA)_{1-x}PbI_3$ 4% (c) perovskite thin films for one-week under 85% humidity atmosphere. These XRD results and analyses unambiguously demonstrate that the most of the MAPI film decomposed into PbI_2 upon exposure to these stringent conditions. By comparison, $(TPA)_x(MA)_{1-x}PbI_3$ 2% and $(TPA)_x(MA)_{1-x}PbI_3$ 4% showed only little formation of PbI_2 (Figure 9b,c) which affords to maintain both the UV-visible absorption capability (Supporting Informations, Figures S7-S9) and the perovskite film morphology as exhamined by SEM imaging (Supporting Information, Figure S10-12) and photographs of the spin coated perovkite thin films (Supporting Information, Figure S13).

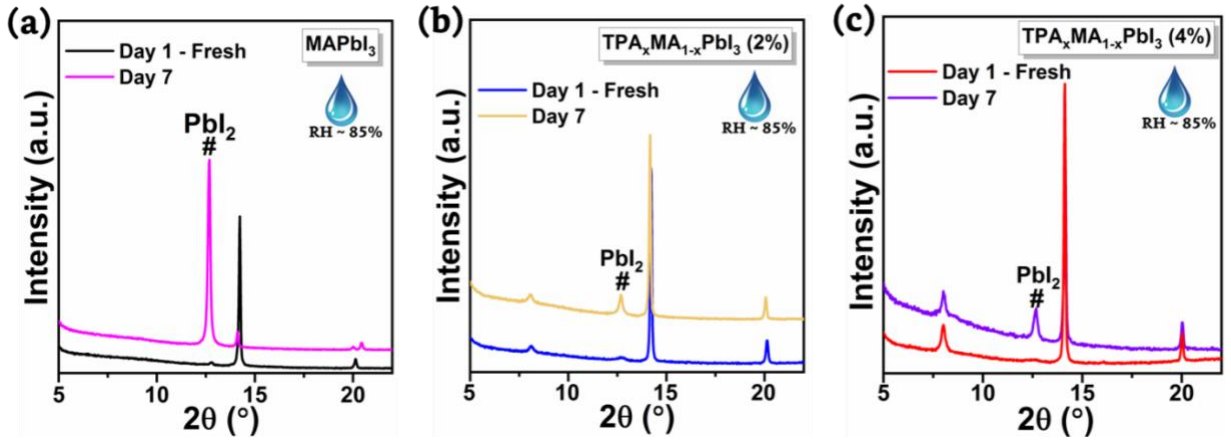

Figure 9. Stability of perovskite films: Comparison of X-ray diffractograms of the perovskite film before and after 7 days storage under 85% humidity chamber for (a) MAPI, (b) $(TPA)_x(MA)_{1-x}PbI_3$ 2%, and (c) $(TPA)_x(MA)_{1-x}PbI_3$ 4%. The films were spin-coated on FTO glass.

CONCLUSIONS

To summarize, we report that the addition of low molar fractions of quaternary ammonium TPA^+ cation in CH_3NH_3I and PbI_2 precursor solution leads to a mesostructured film consisting of smaller, better packed and defect passivated $CH_3NH_3PbI_3$ nanocrystals. XRD and PL studies revealed that the mesostructured film consists of type-I heterostructure of MAPI in association with a lower-dimensional $TPAPb_4I_9$ intermediate phase forming likely at grain boundaries. The XRD results are complemented by 2D ^1H solid-state NMR measurements, which showed nanoscale proximities between TPA^+ and MA^+ cations in $TPA_xMA_{1-x}PbI_3$ 4%. As a result from the incorporation of TPA^+, the film's homogeneity is significantly improved in both terms of photoluminescence yield and excited-state lifetime as demonstrated by FLIM imaging experiments. Devices based on TPA are exhibiting more than 17% power conversion efficiency under A.M. 1.5G conditions, a value at a similar level of the controlled MAPI-devices. However, with respect to MAPI, $TPA_xMA_{1-x}PbI_3$ exhibits a remarkable improvement in absorber stability regardless of the external ageing conditions (temperature, light, atmosphere). This work validates that specifically developed organic monovalent cation judiciously incorporated into 3D perovskite is a credible approach to improve perovskite solar cell performance and above all stability.

METHODS

Materials: Unless specified otherwise, all chemicals were purchased from Sigma-Aldrich. Mesoporous TiO_2 paste, MAI and FK209 were purchased from Dyesol. PbI_2 was purchased from Tokyo Chemical Industry Europe (TCI France).

Device Fabrication: FTO glass substrate (NSG10) was cleaned with 2 vol % hellmanex solution in DI water, isopropanol (Sigma-Aldrich), acetone (Sigma- Aldrich) and treated with UV ozone cleaner for 15 min. To make a compact TiO_2 blocking layer, the cleaned FTO glasses were coated with 0.15 M titanium diisopropoxide bis(acetylacetonate) (75% Aldrich) in 1-butanol (Aldrich) solution by spin-coating at 3000 rpm for 30 s and was heated at 125 ºC for 5 min. After the coated film was cooled down to room temperature, the same process was repeated with 0.3 M titanium diisopropoxide bis(acetylacetonate) solution in 1-butanol. After this, the substrates were heated at 450 ºC for 30 min to form a dense layer of TiO_2. A ~200 nm mesoporous TiO_2 was coated on the substrate by spin coating at a speed of 4000 rpm for 30 s with a ramp-up of 1000 rpm/s from a commercially available TiO_2 paste (Dyesol-30NRD) in ethanol. The weight ratio of TiO_2 paste to ethanol is 6:1. After spin coating, the substrate was immediately dried on a hot plate at 100 °C, and the substrates were then sintered at 500 °C for 30 min before the deposition of the perovskite layer. The precursor solution was prepared by dissolving 1 M MAI (159 mg) and 1.09 M PbI_2 (502.9 mg) in anhydrous N,N-dimethylformamide (0.8 mL, Sigma-Aldrich) and anhydrous dimethylsulfoxide (0.2 ml, Sigma-Aldrich). These solutions were then spin-coated on the substrate in a two-step procedure at 1000 rpm for 10 s and 4000 rpm for 20 s, respectively. During the second step, 1 ml of toluene was dropped 10 s before the end of the program. These spin-coated perovskite films were annealed at 110 °C for 30 min inside Ar-filled glovebox. The HTM was further deposited by spin coating at 3000 rpm for 30 s. The HTM solution was prepared by dissolving 91 mg of Spiro-OMeTAD (Merck) with additives in 1 ml of chlorobenzene. The additives were 21 µl of Li-bis(trifluoromethanesulfonyl) imide from the stock solution (520 mg in 1 ml of acetonitrile), 16 µl of FK209 [tris(2-(1H-pyrazol-1-yl)-4-tert-butylpyridine)-cobalt(III) tris-(bis (trifluoromethylsulfonyl)imide] (375 mg in 1 ml of

acetonitrile) and 36 µl of 4-tertbutylpyridine. The final step was the deposition of the 80 nm thick Au electrode at a rate of ~ 0.3 Å/s by thermal evaporation using MBraun ProVap 4G evaporator. *Characterization*: The perovskite samples for characterization were prepared following exactly the same procedure as for the device fabrication. The XRD experiments were conducted on a Bruker AXS (D8 ADVANCE) diffractometer with Cu Kα radiation (λ = 1.54 Å). Scanning electron microscopy images were obtained using a FEI Quanta 200 FEG microscope. UV-Vis absorption spectra were recorded in a transmittance mode using a Cary5000 UV-Vis-NIR spectrometer. TCSPC experiments were carried out on Edinburgh Instrument FLS980 spectrometer using picosecond 475 nm laser diodes as an excitation source (2 MHz) and a microchannel plate photomultiplier tube (MCP-PMT) Hamamatsu detector set after the first emission monochromator. The measurements were carried out in front-face. The typical instrument response function (IRF) value in this configuration was in the range from 80 to 90 ps. The slit opening of excitation monochromator was 10 nm wide. The steady-state PL spectra were measured using same spectrometer with a continuous xenon arc lamp (450 W) for excitation in a double excitation / double emission monochromator setup to bring stray light rejection to less than 10^{-10}. The slit width was 3 nm. For this, the samples were excited at 450 nm and the emission was detected by a high-gain photomultiplier tube (PMT) detector mounted after the second emission monochromator. For both steady-state PL and TCSPC measurements, the perovskites were deposited on clean glass substrates and the samples were excited from front side, i.e. perovskite side. Fluorescence lifetime images were obtained using a homemade microscope. The excitation light was obtained using a picosecond laser from picoquant at 470 nm (laser head LDH-P-C-470 with a collimator and controlled by a pulse diode laser driver unit PDL 800-B). The excitation light was going through a beam expander to overfill the aperture of

the objective and a bereck compensator (5540, New Focus) was also used to get a circular polarization. The excitation light was directed into an inverted Olympus IX81 and focused on the sample using a dichroic mirror (Semrock BrightLine R488) and an air objective (UplanSapo, 40×, N.A. 0.95). The fluorescence was collected by the same objective lens, directed by the dichroic mirror, passed through the confocal pinhole (100µm), and filtered out by a long pass emission filter (Semrock BrightLine LP 496 nm) before being directed to an avalanche photodiode-based single-photon counting modules (MPD, 50 mm, Grade D, < 50 cps and IRF of 50 ps). The sample was mounted on a three-dimensional translation stage (E-725, Physik Instrument) which allows scanning pixel-by-pixel an entire area on the sample of 24 × 24 µm (8 µm variation in z-axis) and controlled by Symphotime (Picoquant). Photon arrival time for each pixels was obtained using a Picoharp300 and calculation of average lifetime for each pixel was done by Symphotime. Pixel dwell time was fixed to 5 ms to avoid any photo-degradation of the film during acquisition. For average lifetime, images (128 x 128 pixels) were rebinned by 4 to get enough photon statics and only pixels that have more than 500 counts/s were fitted. An average lifetime in intensity was calculated from a reconvoluted fit of IRF (scatter of laser) and a sum of 4 exponential decays. Note that for FLIM experiments, the laser fluence is about 10 times higher than sun irradiation which leads to an increase of bimolecular recombination and give a multiexponential decay.

The powdered TPAI precursor and th scratched-off thin films of $TPA_xMA_{1-x}PbI_3$ 4% obtained from 15 spin-coated substrates were separately packed into 1.3 mm (outer diameter) rotors fitted close with Vespel® caps. All 1D and 2D ^1H NMR experiments were carried out at room temperature on a 18.8 T Bruker AVANCE NEO spectrometer equipped with 1.3 mm double-resonance H/X MAS probe. The sample was spun at a frequency of 35 kHz, except in Figure 3b.

Single-pulse ^{1}H MAS NMR experiments are carried out by co-adding 512 transients with a relaxation delay of 2 s, corresponding to a total experimental time of 18 minutes each. The 2D ^{1}H-^{1}H spin-diffusion (SD) spectra were acquired using 400 t_1 increments, each by co-adding 16 transients, using the States method to achieve sign discrimination in F_1 dimension with a rotor-synchronized t_1 increment of 16.6 µs. The 2D ^{1}H-^{1}H SD spectra were acquired using 1 ms, 10 ms, 100 ms and 500 ms of mixing times, each corresponding to an experimental time of 3.5 h using a relaxation delay of 2 s. The 2D ^{1}H-^{1}H double-quantum (DQ) single-quantum (SQ) spectra were acquired using one rotor period Back-to-Back sequence. [Cite: Feike, M. et al J. Magn. Reson. **1996**, 122A, 214-221; Saalwächter, K.et al., *Journal of Magnetic Resonance* **2011,** *212* (1), 204-215] The DQ coherences were excited and reconverted using a16-step phase cycle. 2D ^{1}H-^{1}H DQ-SQ spectra were acquired using 128 t_1 increments, each by co-adding 16 transients, using the States method to achieve sign discrimination in F_1 dimension with a rotor-synchronized t_1 increment of 16.6 µs, corresponding to an overall experimental time of 2.5 h using a 2 s recycle delay. The ^{1}H chemical shifts are calibrated with respect to neat TMS using adamantane as an external reference (^{1}H resonance, 1.85 ppm).

Current density-voltage (J–V) characteristics of PSCs were recorded by means of a Keithley computer-controlled digital sourcemeter (2412A) combined with a 3A class Newport SOL3A sun simulator with an A.M. 1.5G filter (100 mWcm^{-2}). The light intensity was calibrated with an NREL-certified KG5-filtered Si reference diode. The solar cells were masked (3D printed mask) with an aperture of 0.09 cm^2 to define the active area. UPS measurements were performed using a helium discharge lamp in an Escalab 250Xi spectrometer from Thermo. UPS spectra were recorded with the following parameters: HeI at 21.22 eV, sample bias −10 V and pass energy of 2 eV. The binding energy for UPS was calibrated using the Fermi edge of sputtered cleaned gold

substrate. UPS measurements are very sensitive to the surface (probing depth ~2 nm). Since the preparation of the samples was not performed *in situ*, their exposition to air induces adventitious carbon adsorption on their surface which prevents correct UPS analysis. In order to remove this contamination, we use an Ar cluster gun (8 kV, 2000 atoms) to gently clean the surface inside the spectrometer prior to UPS analysis. These large Ar clusters are able to remove organic contamination without destroying the perovskite structure.

Stability testing: In this work, we did three kinds of stability tests carried out under open-circuit conditions. The first set of stability test was done in an argon atmosphere. The devices were stored in an argon-filled glovebox and were taken periodically for I-V measurements that were done in ambient condition. For the second set of stability test, the devices were stored in ambient air and light with a relative humidity of 55±5% and temperature of 20±5 °C. The third test to check thermal stability was done at 60 °C in an argon atmosphere. Devices were put on a ceramic hot plate at 60 °C in the argon-filled glovebox and were taken out every 72 h for I-V measurements, which was done in ambient conditions. For stability testing for perovskites films, the films were stored for a week in an in-house-built humidity chamber with ~85% relative humidity.

ASSOCIATED CONTENT

The Supporting Information is available free of charge on the ACS Publications website The following files are available free of charge. Figure S1. XRD pattern of the resulting film spin-coated on glass with 1:1, 1:2 and 1:4 ratio between TPAI and PbI_2. Figure S2. X-ray Diffraction pattern of TPAI film obtained by spin-coating on the glass. Figure S3. UV-visible absorption spectrum and corresponding Tauc-plot for $(TPA)Pb_4I_9$ film spin-coated on glass. Figure S4. Photoluminescence mapping of $MAPbI_3$, $TPA_xMA_{1-x}PbI_3$ (2%) and $TPA_xMA_{1-x}PbI_3$ (4%). Figure S5. The PL lifetime histogram of the samples extracted from FLIM images. Figure S6. UV-visible absorption spectrum measured in transmittance for fresh $MAPbI_3$ film and after 7

days storage at room temperature under 85% humidity level. The films were spin-coated upon FTO glass. Figure S7. UV-visible absorption spectrum measured in transmittance for fresh $TPA_xMA_{1-x}PbI_3$ (2%) film and after 7 days storage at room temperature under 85% humidity level. The films were spin-coated upon FTO glass. Figure S8. UV-visible absorption spectrum measured in transmittance for fresh $TPA_xMA_{1-x}PbI_3$ (4%) film and after 7 days storage at room temperature under 85% humidity level. The films were spin-coated upon FTO glass. Figure S9. SEM image of the fresh $MAPbI_3$ film and after 7 days storage at room temperature under 85% humidity level. Figure S10. SEM image of the fresh $TPA_xMA_{1-x}PbI_3$ (2%) film and after 7 days storage at room temperature under 85% humidity level. Figure S11. SEM image of the fresh $TPA_xMA_{1-x}PbI_3$ (4%) film and after 7 days storage at room temperature under 85% humidity level. Figure S12. Photograph showing comparison of $MAPbI_3$, $TPA_xMA_{1-x}PbI_3$ (2%) and $TPA_xMA_{1-x}PbI_3$ (4%) films stored at room temperature under 85% relative humidity level for 7 days. The films were spin-coated on FTO glass.

AUTHOR INFORMATION

Corresponding Author

Email: frederic.sauvage@u-picardie.fr (F.S)

Present Addresses

Anurag Krishna (A.K.) is presently at Laboratory of Photomolecular Science, Ecole Polytechnique Fédérale de Lausanne, 1015 Lausanne, Switzerland

Author Contributions

A.K. assembled devices, optimized performances and carried out stability testing in association with M.A.A.K. G. N. M. R. carried out solid-state NMR experiments. A.K. and F.S. carried out PL and TCPSC experiments. M.T.D. and M.S. performed FLIM experiments. A.F. performed

UPS analysis. All authors have contributed to the scientific discussion. A.K. and F.S. have prepared and finalized the manuscript.

Notes

The authors declare no competing financial interest

ACKNOWLEDGMENT

F.S. wish to thank H2020 research and innovation program for IMPRESSIVE project under grant agreement n°826013 and region Hauts-de-France, FEDER and EDF for PhD grants of M.A. and A.K. M.S. is indebted to the Chevreul Institute (FR 2638) and the Agence National de la Recherche (ANR-14-CE08-0015-01 Ultrafast Nanoscopy) for financial support. Chevreul Institute (FR 2638), Ministère de l'Enseignement Supérieur, de la Recherche et de l'Innovation, Hauts-de-France Region and FEDER are acknowledged for supporting and funding partially this work. G.N.M.R, L.D and O.L. gratefully acknowledge the financial support from the IR-RMN-THC FR-3050 CNRS France for conducting solid-state NMR measurements.

.

REFERENCES

(1) Lee, M. M.; Teuscher, J.; Miyasaka, T.; Murakami, T. N.; Snaith, H. J. Efficient Hybrid Solar Cells Based on Meso-Superstructured Organometal Halide Perovskites. *Science (80-.).* **2012**.

(2) Kim, H. S.; Lee, C. R.; Im, J. H.; Lee, K. B.; Moehl, T.; Marchioro, A.; Moon, S. J.; Humphry-Baker, R.; Yum, J. H.; Moser, J. E.; et al. Lead Iodide Perovskite Sensitized All-Solid-State Submicron Thin Film Mesoscopic Solar Cell with Efficiency Exceeding 9%. *Sci. Rep.* **2012**, *2*, 1–7.

(3) Xing, G.; Mathews, N.; Sun, S.; Lim, S. S.; Lam, Y. M.; Graẗzel, M.; Mhaisalkar, S.; Sum, T. C. Long-Range Balanced Electron-and Hole-Transport Lengths in Organic-Inorganic $CH_3NH_3PbI_3$. *Science (80-.).* **2013**, *342* (6156), 344–347.

(4) Saparov, B.; Mitzi, D. B. Organic-Inorganic Perovskites: Structural Versatility for Functional Materials Design. *Chemical Reviews*. **2016**, 4558–4596.

(5) Jeon, N. J.; Noh, J. H.; Yang, W. S.; Kim, Y. C.; Ryu, S.; Seo, J.; Seok, S. Il. Compositional Engineering of Perovskite Materials for High-Performance Solar Cells. *Nature* **2015**, *517* (7535), 476–480.

(6) NREL Efficiency Chart https://www.nrel.gov/pv/assets/images/efficiency-chart.png.

(7) Snaith, H. J. Present Status and Future Prospects of Perovskite Photovoltaics. *Nat. Mater.* **2018**, *17* (5), 372–376.

(8) Manser, J. S.; Saidaminov, M. I.; Christians, J. A.; Bakr, O. M.; Kamat, P. V. Making and Breaking of Lead Halide Perovskites. *Acc. Chem. Res.* **2016**, *49* (2), 330–338.

(9) Niu, G.; Guo, X.; Wang, L. Review of Recent Progress in Chemical Stability of Perovskite Solar Cells. *J. Mater. Chem. A* **2015**, *3* (17), 8970–8980.

(10) Slavney, A. H.; Smaha, R. W.; Smith, I. C.; Jaffe, A.; Umeyama, D.; Karunadasa, H. I. Chemical Approaches to Addressing the Instability and Toxicity of Lead-Halide Perovskite Absorbers. *Inorg. Chem.,* **2017**, 46–55.

(11) Conings, B.; Drijkoningen, J.; Gauquelin, N.; Babayigit, A.; D'Haen, J.; D'Olieslaeger, L.; Ethirajan, A.; Verbeeck, J.; Manca, J.; Mosconi, E.; et al. Intrinsic Thermal Instability of Methylammonium Lead Trihalide Perovskite. *Adv. Energy Mater.* **2015**, *5* (15), 1–8.

(12) Saliba, M.; Matsui, T.; Seo, J. Y.; Domanski, K.; Correa-Baena, J. P.; Nazeeruddin, M. K.; Zakeeruddin, S. M.; Tress, W.; Abate, A.; Hagfeldt, A.; et al. Cesium-Containing

Triple Cation Perovskite Solar Cells: Improved Stability, Reproducibility and High Efficiency. *Energy Environ. Sci.* **2016**, *9* (6), 1989–1997.

(13) Correa-Baena, J.-P.; Saliba, M.; Buonassisi, T.; Grätzel, M.; Abate, A.; Tress, W.; Hagfeldt, A. Promises and Challenges of Perovskite Solar Cells. *Science (80-.).* **2017**, *358* (6364), 739 – 744.

(14) Zheng, X.; Chen, B.; Dai, J.; Fang, Y.; Bai, Y.; Lin, Y.; Wei, H.; Zeng, X. C.; Huang, J. Defect Passivation in Hybrid Perovskite Solar Cells Using Quaternary Ammonium Halide Anions and Cations. *Nat. Energy* **2017**, *2* (7), 17102.

(15) Wang, Q.; Chen, B.; Liu, Y.; Deng, Y.; Bai, Y.; Dong, Q.; Huang, J. Scaling Behavior of Moisture-Induced Grain Degradation in Polycrystalline Hybrid Perovskite Thin Films. *Energy Environ. Sci.* **2017**, *10* (2), 516–522.

(16) Yang, B.; Dyck, O.; Poplawsky, J.; Keum, J.; Puretzky, A.; Das, S.; Ivanov, I.; Rouleau, C.; Duscher, G.; Geohegan, D.; et al. Perovskite Solar Cells with Near 100% Internal Quantum Efficiency Based on Large Single Crystalline Grains and Vertical Bulk Heterojunctions. *J. Am. Chem. Soc.* **2015**, *137* (29), 9210–9213.

(17) Krishna, A.; Gottis, S.; Nazeeruddin, M. K.; Sauvage, F. Mixed Dimensional 2D/3D Hybrid Perovskite Absorbers: The Future of Perovskite Solar Cells? *Adv. Funct. Mater.* **2019**, *29* (8), 1806482.

(18) Chen, Y.; Sun, Y.; Peng, J.; Tang, J.; Zheng, K.; Liang, Z. 2D Ruddlesden-Popper Perovskites for Optoelectronics. *Advanced Materials*. **2017**, 1–15.

(19) Slavney, A. H.; Smaha, R. W.; Smith, I. C.; Jaffe, A.; Umeyama, D.; Karunadasa, H. I. Chemical Approaches to Addressing the Instability and Toxicity of Lead-Halide Perovskite Absorbers. *Inorg. Chem.* **2017**, *56* (1), 46–55.

(20) Smith, I. C.; Hoke, E. T.; Solis-Ibarra, D.; McGehee, M. D.; Karunadasa, H. I. A Layered Hybrid Perovskite Solar-cell Absorber with Enhanced Moisture Stability. *Angew. Chemie* **2014**, *126* (42), 11414–11417.

(21) Cao, D. H.; Stoumpos, C. C.; Farha, O. K.; Hupp, J. T.; Kanatzidis, M. G. 2D Homologous Perovskites as Light-Absorbing Materials for Solar Cell Applications. *J. Am. Chem. Soc.* **2015**, *137* (24), 7843–7850.

(22) Ma, C.; Shen, D.; Ng, T. W.; Lo, M. F.; Lee, C. S. 2D Perovskites with Short Interlayer Distance for High-Performance Solar Cell Application. *Adv. Mater.* **2018**, *30* (22), 2–7.

(23) Tsai, H.; Nie, W.; Blancon, J.-C.; Stoumpos, C. C.; Asadpour, R.; Harutyunyan, B.; Neukirch, A. J.; Verduzco, R.; Crochet, J. J.; Tretiak, S.; et al. High-Efficiency Two-Dimensional Ruddlesden–Popper Perovskite Solar Cells. *Nature* **2016**, *536* (7616), 312–316.

(24) Koh, T. M.; Shanmugam, V.; Schlipf, J.; Oesinghaus, L.; Müller-Buschbaum, P.; Ramakrishnan, N.; Swamy, V.; Mathews, N.; Boix, P. P.; Mhaisalkar, S. G. Nanostructuring Mixed-Dimensional Perovskites: A Route Toward Tunable, Efficient Photovoltaics. *Adv. Mater.* **2016**, *28* (19), 3653–3661.

(25) Ye, T.; Bruno, A.; Han, G.; Koh, T. M.; Li, J.; Jamaludin, N. F.; Soci, C.; Mhaisalkar, S. G.; Leong, W. L. Efficient and Ambient-Air-Stable Solar Cell with Highly Oriented 2D@3D Perovskites. *Adv. Funct. Mater.* **2018**, *1801654*, 1–8.

(26) Cho, Y.; Soufiani, A. M.; Yun, J. S.; Kim, J.; Lee, D. S.; Seidel, J.; Deng, X.; Green, M. A.; Huang, S.; Ho-Baillie, A. W. Y. Mixed 3D–2D Passivation Treatment for Mixed-Cation Lead Mixed-Halide Perovskite Solar Cells for Higher Efficiency and Better Stability. *Adv. Energy Mater.* **2018**, *8* (20), 1–10

(27) Poli, I.; Eslava, S.; Cameron, P. Tetrabutylammonium Cations for Moisture-Resistant and Semitransparent Perovskite Solar Cells. *J. Mater. Chem. A* **2017**, *00*, 1–9.

(28) Grancini, G.; Roldán-Carmona, C.; Zimmermann, I.; Mosconi, E.; Lee, X.; Martineau, D.; Narbey, S.; Oswald, F.; De Angelis, F.; Graetzel, M.; et al. One-Year Stable Perovskite Solar Cells by 2D/3D Interface Engineering. *Nat. Commun.* **2017**, *8*, 1–8.

(29) Wang, Z.; Lin, Q.; Chmiel, F. P.; Sakai, N.; Herz, L. M.; Snaith, H. J. Efficient Ambient-Air-Stable Solar Cells with 2D-3D Heterostructured Butylammonium-Caesium-Formamidinium Lead Halide Perovskites. *Nat. Energy* **2017**, *2* (9), 1–10.

(30) Naphade, R.; Zhao, B.; Richter, J. M.; Booker, E.; Krishnamurthy, S.; Friend, R. H.; Sadhanala, A.; Ogale, S. High Quality Hybrid Perovskite Semiconductor Thin Films with Remarkably Enhanced Luminescence and Defect Suppression via Quaternary Alkyl Ammonium Salt Based Treatment. *Adv. Mater. Interfaces* **2017**, *4* (19), 1–8.

(31) Shih, Y. C.; Lan, Y. B.; Li, C. S.; Hsieh, H. C.; Wang, L.; Wu, C. I.; Lin, K. F. Amino-Acid-Induced Preferential Orientation of Perovskite Crystals for Enhancing Interfacial Charge Transfer and Photovoltaic Performance. *Small* **2017**, *13* (22), 1–10.

(32) Docampo, P.; Hanusch, F. C.; Giesbrecht, N.; Angloher, P.; Ivanova, A.; Bein, T. Influence of the Orientation of Methylammonium Lead Iodide Perovskite Crystals on Solar Cell Performance. *APL Mater.* **2014**, *2* (8).

(33) Chen, A. Z.; Foley, B. J.; Ma, J. H.; Alpert, M. R.; Niezgoda, J. S.; Choi, J. J. Crystallographic Orientation Propagation in Metal Halide Perovskite Thin Films. *J. Mater. Chem. A* **2017**, *5* (17), 7796–7800.

(34) Jacobsson, T. J.; Correa-Baena, J. P.; Halvani Anaraki, E.; Philippe, B.; Stranks, S. D.; Bouduban, M. E. F.; Tress, W.; Schenk, K.; Teuscher, J.; Moser, J. E.; et al. Unreacted

PbI_2 as a Double-Edged Sword for Enhancing the Performance of Perovskite Solar Cells. *J. Am. Chem. Soc.* **2016**, *138* (32), 10331–10343.

(35) Kieslich, G.; Sun, S.; Cheetham, A. K. Solid-State Principles Applied to Organic–Inorganic Perovskites: New Tricks for an Old Dog. *Chem. Sci.* **2014**, *5* (12), 4712–4715.

(36) Li, W.; Wang, Z.; Deschler, F.; Gao, S.; Friend, R. H.; Cheetham, A. K. Chemically Diverse and Multifunctional Hybrid Organic-Inorganic Perovskites. *Nat. Rev. Mater.* **2017**, *2* (3).

(37) Nilsson, E. J.; Alfredsson, V.; Bowron, D. T.; Edler, K. J. A Neutron Scattering and Modelling Study of Aqueous Solutions of Tetramethylammonium and Tetrapropylammonium Bromide. *Phys. Chem. Chem. Phys.* **2016**, *18* (16), 11193–11201.

(38) De Wolf, S.; Holovsky, J.; Moon, S. J.; Löper, P.; Niesen, B.; Ledinsky, M.; Haug, F. J.; Yum, J. H.; Ballif, C. Organometallic Halide Perovskites: Sharp Optical Absorption Edge and Its Relation to Photovoltaic Performance. *J. Phys. Chem. Lett.* **2014**, *5* (6), 1035–1039.

(39) Lee, J. W.; Bae, S. H.; Hsieh, Y. T.; De Marco, N.; Wang, M.; Sun, P.; Yang, Y. A Bifunctional Lewis Base Additive for Microscopic Homogeneity in Perovskite Solar Cells. *Chem* **2017**, *3* (2), 290–302.

(40) Emara, J.; Schnier, T.; Pourdavoud, N.; Riedl, T.; Meerholz, K.; Olthof, S. Impact of Film Stoichiometry on the Ionization Energy and Electronic Structure of $CH_3NH_3PbI_3$ Perovskites. *Adv. Mater.* **2016**, *28* (3), 553–559.

(41) Wang, R.; Zhuo, M. P.; Li, J.; Zhai, T.; Yang, J.; Fu, K.; Liao, L. S.; Liu, L.; Duhm, S. Surface $CH_3NH_3^+$ to CH_3^+ Ratio Impacts the Work Function of Solution-Processed and Vacuum-Sublimed $CH_3NH_3PbI_3$ Thin Films. *Adv. Mater. Interfaces* **2019**, *6* (6), 1–8.

(42) Yin, W. J.; Shi, T.; Yan, Y. Unusual Defect Physics in CH3NH3PbI3 Perovskite Solar Cell Absorber. *Appl. Phys. Lett.* **2014**, *104* (6).

(43) Zu, F.; Amsalem, P.; Egger, D. A.; Wang, R.; Wolff, C. M.; Fang, H.; Loi, M. A.; Neher, D.; Kronik, L.; Duhm, S.; et al. Constructing the Electronic Structure of CH 3 NH 3 PbI 3 and CH 3 NH 3 PbBr 3 Perovskite Thin Films from Single-Crystal Band Structure Measurements. *J. Phys. Chem. Lett.* **2019**, *10* (3), 601–609.

(44) Endres, J.; Egger, D. A.; Kulbak, M.; Kerner, R. A.; Zhao, L.; Silver, S. H.; Hodes, G.; Rand, B. P.; Cahen, D.; Kronik, L.; et al. Valence and Conduction Band Densities of States of Metal Halide Perovskites: A Combined Experimental-Theoretical Study. *J. Phys. Chem. Lett.* **2016**, *7* (14), 2722–2729.

(45) Son, D. Y.; Lee, J. W.; Choi, Y. J.; Jang, I. H.; Lee, S.; Yoo, P. J.; Shin, H.; Ahn, N.; Choi, M.; Kim, D.; et al. Self-Formed Grain Boundary Healing Layer for Highly Efficient $CH_3NH_3PbI_3$ Perovskite Solar Cells. *Nat. Energy* **2016**, *1* (7), 1–8.

(46) Dong; Shi; Valerio; Adinolfi; Riccardo; Comin; Mingjian; Yuan; Erkki; Alarousu; et al. Low Trap-State Density and Long Carrier Diffusion in Organolead Trihalide Perovskite Single Crystals. *Science (80-.).* **2015**, *347* (6221), 519–522.

(47) de Quilettes, D. W.; Vorpahl, S. M.; Stranks, S. D.; Nagaoka, H.; Eperon, G. E.; Ziffer, M. E.; Snaith, H. J.; Ginger, D. S. Impact of Microstructure on Local Carrier Lifetime in Perovskite Solar Cells. *Science (80-.).* **2015**, *348* (6235), 683–686.

(48) Dequilettes, D. W.; Koch, S.; Burke, S.; Paranji, R. K.; Shropshire, A. J.; Ziffer, M. E.; Ginger, D. S. Photoluminescence Lifetimes Exceeding 8 Ms and Quantum Yields Exceeding 30% in Hybrid Perovskite Thin Films by Ligand Passivation. *ACS Energy Lett.* **2016**, *1* (2), 438–444.

(49) Merdasa, A.; Kiligaridis, A.; Rehermann, C.; Abdi-Jalebi, M.; Stöber, J.; Louis, B.; Gerhard, M.; Stranks, S.D.; Unger, E.L.; Scheblykin, I.G. Impact of Excess Lead Iodide on the Recombination Kinetics in Metal Halide Perovskites. *ACS Energy Lett.* **2019**, *4*, 1370−1378.

(50) Agrawal, A.; Dar, T. A.; Phase, D. M.; Sen, P. Type I and Type II Band Alignments in ZnO/MgZnO Bilayer Films. *Appl. Phys. Lett.* **2014**, *105* (8), 81603.

(51) Liu, B.; Long, M.; Cai, M.; Ding, L.; Yang, J. Interfacial Charge Behavior Modulation in 2D/3D Perovskite Heterostructure for Potential High-Performance Solar Cells. *Nano Energy* **2019**, *59*, 715–720.

(52) Braly, I. L.; deQuilettes, D. W.; Pazos-Outón, L. M.; Burke, S.; Ziffer, M. E.; Ginger, D. S.; Hillhouse, H. W. Hybrid Perovskite Films Approaching the Radiative Limit with over 90% Photoluminescence Quantum Efficiency. *Nat. Photonics* **2018**, *12* (6), 355–361.

(53) Domanski, K.; Alharbi, E. A.; Hagfeldt, A.; Grätzel, M.; Tress, W. Systematic Investigation of the Impact of Operation Conditions on the Degradation Behaviour of Perovskite Solar Cells. *Nat. Energy* **2018**, *3* (1), 61–67.

(54) Wang, R.; Xue, J.; Meng, L.; Lee, J.-W.; Zhao, Z.; Sun, P.; Cai, L.; Huang, T.; Wang, Z.; Wang, Z.-K.; et al. Caffeine Improves the Performance and Thermal Stability of Perovskite Solar Cells. *Joule* **2019**, 1–14.

(55) Wang, R.; Mujahid, M.; Duan, Y.; Wang, Z.-K.; Xue, J.; Yang, Y. A Review of Perovskites Solar Cell Stability. *Adv. Funct. Mater.* **2019**, *0* (0), 1808843.

(56) Krishna, A.; Grimsdale, A. C. Hole Transporting Materials for Mesoscopic Perovskite Solar Cells – towards a Rational Design? *J. Mater. Chem. A* **2017**, *5* (32), 16446–16466.

TOC

Defect passivation and stability enhancement in lead halide perovskite via incorporation of tetrapropylammonium cation

Anurag Krishna[†], *Mohammad Ali Akhavan Kazemi*[†], *Mai Trang Do*[‡], *Michel Sliwa*[‡], *G. N. Manjunatha Reddy*[§], *Laurent Delevoye*[§], *Olivier Lafon*[§], *Alexandre Felten*[#], *Sébastien Gottis*[†], *and Frédéric Sauvage*[†]*

Keywords: Stable Perovskites, Defect Passivation, 2D perovskites, molecular engineering

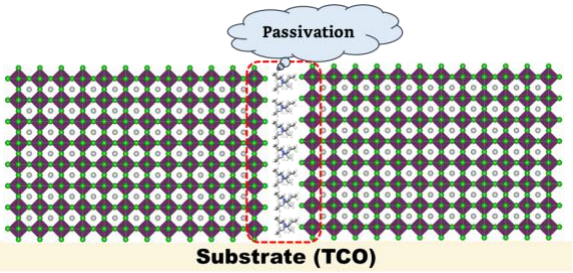

Stable perovskite thin films and solar cells are obtained by judicious incorporation of multifunctional tetrapropylammonium (TPA) cations in methylammonium iodide ($MAPbI_3$). Upon addition of TPA, a heterostructure is formed which leads to passivation of defects along with improved morphology. This study highlights a new strategy to enhance the stability of PSCs while maintaining high performance.